RSC Advances

PAPER

View Article Online
View Journal | View Issue

Check for updates

Cite this: *RSC Adv.*, 2024, **14**, 37676

Enhancing the capacity of Mn-rich cathodes by kinetics control for lithium-ion batteries†

Jue Wu, *[a] Weiping Gao,[a] Qiling Wen,[a] Zhipeng Zhuang[a] and Liangkui Zhu[b]

High energy density cathodes have been widely explored in recent years in the area of lithium-ion batteries, which suffer from sluggish kinetics and structural degradation. Herein, the kinetics of the charge transfer process on the cathode material was accelerated *via* synergistic lanthurizing and Li/Mn optimization method, thereby delivering layered-spinel biphase and improved electrochemical performance. The available capacity was greatly enhanced from 57.4 mA h g^{-1} for the pristine material to 233.4 mA h g^{-1} for the modified material with a voltage of 1.5–4.8 V. Based on the electrochemical and structural characterization, the improved capacity and rate performance were attributed to the engineered structural design with enhanced electrochemical kinetics. Electrochemical impedance spectroscopy results indicated that modification tuning could effectively lower the activation energy of the charge transfer process by nearly 45%. This synergistic approach widens the method for enhancing the energy density of oxide cathodes.

Received 21st August 2024
Accepted 21st October 2024

DOI: 10.1039/d4ra06047d

rsc.li/rsc-advances

Open Access Article. Published on 25 November 2024. Downloaded on 2/10/2026 6:33:09 PM.
This article is licensed under a Creative Commons Attribution-NonCommercial 3.0 Unported Licence.

Introduction

Lithium-ion batteries with high energy density rely on the high-voltage operation of oxide cathodes to gain extra capacity.[1,2] Mn-rich cathode has been proposed as a replacement for the commercial layered cathode as it is inexpensive and safer.[3,4] Unfortunately, the poor kinetics and structural stability lead to a severe decrease in the rate performance and capacity, thus hindering further commercial applications.[5–7] The main reason affecting the electrochemical performance of Mn-rich oxide material is kinetics.[8–10] The charge compensation at high voltage for oxygen anion and transition metal (TM) cation bi-center redox increases the available capacity.[10,11] However, with a high ratio of lithium (de)intercalation, the oxygen atoms become unstable. The undesirable oxygen gas released from the cathode material directly reduces the available capacity.[12,13] Because the organic electrolyte is chemically reactive at high voltage, the cathode/electrolyte side reaction could still lose oxygen atoms and thicken the cathode electrolyte interphase (CEI). Therefore, the undesired oxygen side reaction leads to sluggish kinetics, leading to poor lithium-ion diffusion at high voltage.[14,15] It further results in fast impedance growth, accelerated structural degradation, and battery failure.

Extensive efforts have been devoted to tackling the issues mentioned above, including the modification of the surface with protective layers,[16–18] design of the cathode structure,[19–21] introduction of functional electrolyte additives,[22] and application of a solid-state electrolyte.[23,24] Doping is one of the most widely used methods to enhance the electrochemical performance of cathode materials. Various dopant elements, such as Al, Ti, Fe, and Mg, have been examined in Mn-rich cathode oxide.[25–27] However, the lithium ion diffusion kinetics and surface stability of the cathodes decrease with increased oxygen redox reaction. In this regard, investigations on the simultaneous modification of the structure and surface with a synergetic strategy have been recently reported.[28]

Herein, an effective engineering strategy is proposed to tailor the Mn-rich Li_2MnO_3 (LMO) cathode material *via* the La–O bond and layered-spinel biphase simultaneously (Fig. 1). Pristine LMO material has been confirmed to present severe oxygen release.[29,30] Replacing the weakly bonded surface oxygen with a stable La–O bond has been proposed to prevent the oxygen release.[31,32] Because of the biphase framework and favorable ionic transport network, the modified Mn-rich material delivers a high specific capacity of 233.4 mA h g^{-1}. Based on X-ray diffraction (XRD), transmission electron microscopy (TEM), and Raman spectroscopy, the modified Mn-rich material presents a layered-spinel biphase. The galvanostatic intermittent titration technique (GITT) data and temperature-varied electrochemical impedance spectroscopy (EIS) data analyses demonstrated that the notable improvement in the electrochemical performance is due to the favorable lithium-ion diffusion process. This study emphasizes the importance of fast kinetics on the charge transfer process and provides a promising path for the rational design of LMO materials to achieve high energy density and high rate performance.

[a]*School of Life Sciences, Zhuhai College of Science and Technology, Zhuhai 519041, China*

[b]*State Key Laboratory of Inorganic Synthesis & Preparative Chemistry, Jilin University, Changchun 130012, China. E-mail: jwu@zcst.edu.cn*

† Electronic supplementary information (ESI) available. See DOI: https://doi.org/10.1039/d4ra06047d

© 2024 The Author(s). Published by the Royal Society of Chemistry

Open Access Article. Published on 25 November 2024. Downloaded on 2/10/2026 6:33:09 PM.
This article is licensed under a Creative Commons Attribution-NonCommercial 3.0 Unported Licence.

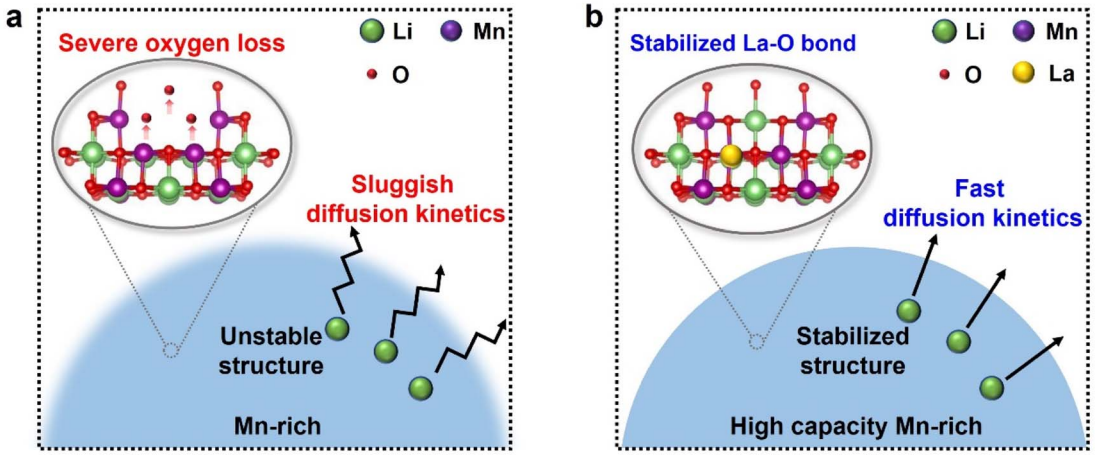

Fig. 1 The Mn-rich cathode cycled at high voltage enables high available capacity. (a) However, high voltage electrochemical cycling leads to severe oxygen loss, which results in sluggish lithium ion diffusion kinetics. (b) Herein, we constructed a highly stable structure with La doping and Li/Mn optimization, which delivers stabilized structure and fast lithium-ion diffusion kinetics.

Experimental

Synthesis of LMO series cathode materials

The cathode materials Li_2MnO_3 (LMO), $Li_2Mn_{0.99}La_{0.01}O_{3-\delta}$ ($La_{0.01}$), $Li_2Mn_{0.97}La_{0.03}O_{3-\delta}$ ($La_{0.03}$), $Li_2Mn_{0.95}La_{0.05}O_{3-\delta}$ ($La_{0.05}$), and $Li_2Mn_{1.97}La_{0.03}O_{5-\delta}$ (LMLO) were synthesized *via* a high-temperature solid-state method. The raw materials Li_2CO_3, MnO_2, and La_2O_3 were placed in an agate tank according to the stoichiometric ratio, soaked in acetone, and mixed *via* ball milling for 3–4 hours. The uniformly mixed slurry was dried and pressed into a sheet at a pressure of 90 MPa and then calcined at 750 °C for 24 hours in a muffle furnace. After the high-temperature calcination, the obtained samples were taken out, ground into powder, and named as the cathode materials. The synthesis of the reference $Li_2Mn_4O_9$ material has been reported in previous works.[33,34] The precursor was calcined at 400 °C for 32 hours in air.

Electrochemical measurement

Aluminum sheet was punched into a circular plate with a diameter of 14 mm and cleaned with 0.1 M NaOH solution and 0.1% $H_2C_2O_4$ solution. Taking the synthesized cathode material as the active material, acetylene black as the conductive agent, and polyvinylidene fluoride (PVDF) as the binder in a weight ratio of 8 : 1 : 1, the mixture was sequentially added into the mill tank with *N*-methyl-2-pyrrolidone (NMP) as the dispersant. The mixture was milled at a high speed of 350 rpm for 2–3 hours to obtain a uniform slurry. The slurry was coated on the treated aluminum sheet and dried at 120 °C in a vacuum drying oven overnight to obtain the cathode electrode. The weight of the active material was 3–5 mg in the cathode electrode.

To test the electrochemical performance, we assembled the CR2032 coin-type cell in a glovebox filled with inert argon gas (H_2O < 0.01 ppm, O_2 < 0.01 ppm). The cells were assembled with a self-made electrode, Celgard 2300 as the separator, lithium metal foil as the counter electrode, and 1.0 M $LiPF_6$ in a mixed solvent (the volume ratio, EC : DEC : EMC = 1 : 1 : 1) as the electrolyte. The galvanostatic charge–discharge test was conducted on a battery cycler (CT-3008W, Neware, China). After standing at room temperature for 8 hours, the cell underwent long-term cycling and electrochemical tests such as rate performance, GITT, *etc.* The EIS and cyclic voltammetry (CV) tests were conducted on the an electrochemical workstation (Shanghai Chenhua CHI760E, and VERSASTAT 4). The frequency range of the EIS test was 0.01 Hz to 100 kHz with a voltage amplitude of ±5 mV. The scanning rate of the CV test was 0.1 mV s^{-1}. The GITT test was conducted with charge/discharge at a current density of 25 mA g^{-1} for 10 minutes and the rest for 40 minutes.

Structural characterization

The XRD data were collected on a Rigaku Ultima IV powder X-ray diffractometer using Cu Kα radiation (λ = 1.5406 Å) source. Rietveld refinement was performed using the General Structure Analysis System (GSAS) software with the EXPGUI interface.[35] Schematic diagrams were drawn using the VESTA software.[36] Raman spectroscopy (Horiba LabRaman HR evolution) was conducted at an activated wavelength of 633 nm and power of 7 mW. The differential scanning calorimetry (DSC) (NETZSCH, STA409PC) measurements for the charged LMO and LMLO electrodes were carried out at a heating rate of 5 °C min^{-1}. The scanning electron microscopy (SEM) and assorted energy dispersive spectroscopy (EDS) measurements were performed (Mira, Tescan) to characterize the morphology of the particle and elemental mapping of the materials. Transmission electron microscopy (TEM) technique was applied using a JEM-2100F TEM instrument. The stoichiometry of the elemental compositions for the cathode materials was examined by inductively coupled plasma atomic emission spectrometry (ICP-AES).

Results and discussion

Structural design and material characterization

The general structural design for the high-capacity Mn-rich cathode is outlined in Fig. 2a. The pristine Li_2MnO_3 (LMO) was viewed as $Li[Li_{1/3}Mn_{2/3}]O_2$, wherein one-third of the

© 2024 The Author(s). Published by the Royal Society of Chemistry

Open Access Article. Published on 25 November 2024. Downloaded on 2/10/2026 6:33:09 PM.
This article is licensed under a Creative Commons Attribution-NonCommercial 3.0 Unported Licence.

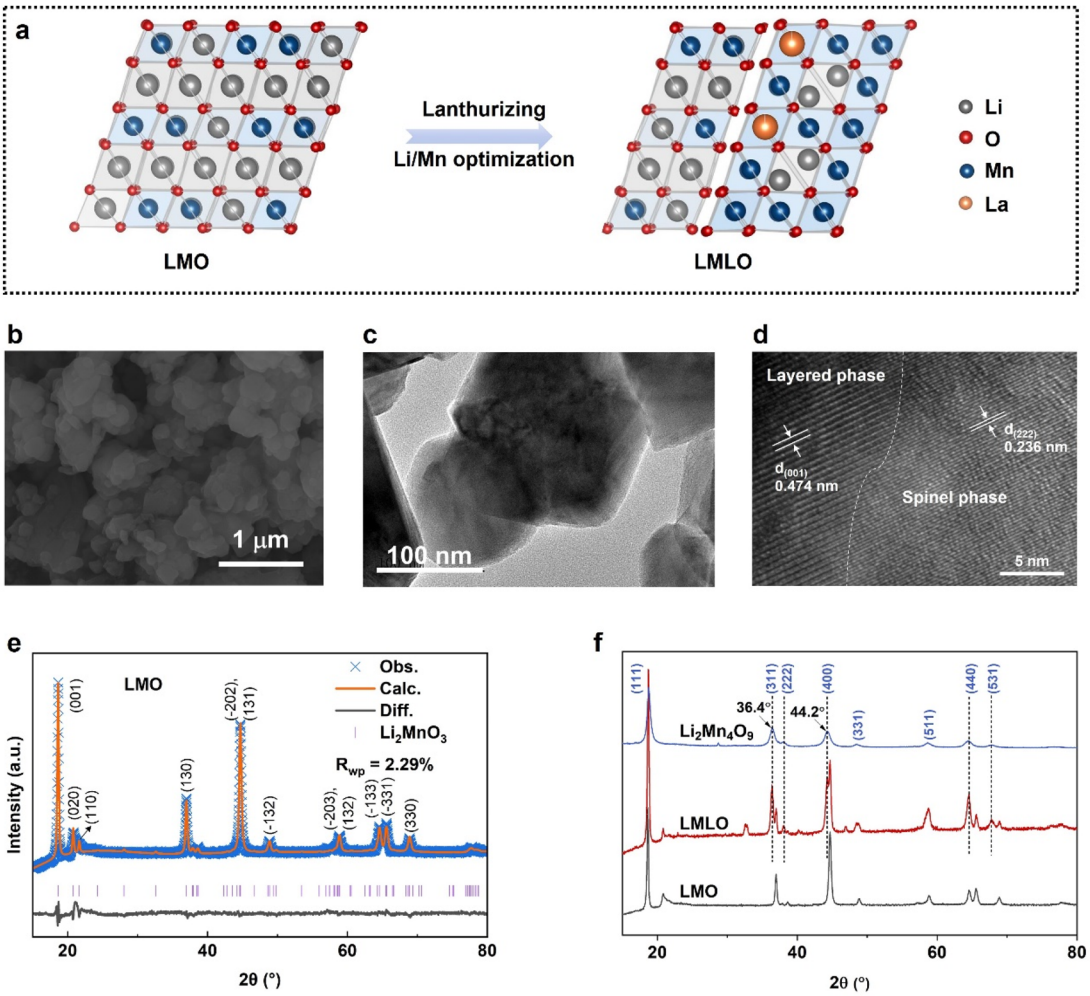

Fig. 2 (a) Proposed crystal atomic structure of the bulk architecture for LMO and LMLO materials. (b) SEM image for the LMLO material. (c and d) TEM image for the LMLO material. (e) XRD patterns and Rietveld refinement for the LMO material. (f) XRD patterns for LMO, LMLO and $Li_2Mn_4O_9$ materials.

transition metal (TM) layer site is occupied by the lithium atom. For the LMLO material, the combination of layered-spinel (Li atom in tetrahedral site) biphase and rare element La doping (with stabilized La–O bond) suggests enhanced structural stability. The pristine LMO and modified materials were synthesized *via* a simple one-step solid-state method.[37]

The SEM images for pristine LMO and modified LMLO material are presented in Fig. S1† and **2b**. It shows that both materials deliver irregular ball shapes with a diameter of 100–200 nm, which is consistent with the TEM image for the LMLO material (Fig. 2c). The coexistence of layered and spinel phases in the LMLO material was characterized *via* the TEM method (Fig. 2d). Lattice fringes in the bulk region with a *d*-spacing of 0.474 nm can be ascribed to the (001) facet of layered structure. In some regions, the transition metal ions occupy part of the lithium-ion layer, forming a crystal plane with a *d*-spacing of 0.236 nm, which is consistent with the (222) facet of the spinel phase (space group $Fd\bar{3}m$).[38,39] The elemental content was detected *via* inductively-coupled plasma-atomic emission spectrometry (ICP-AES). The ICP-AES data (Table 1) indicates that the compositions of the as-synthesized compounds are close to that of the targeted compositions, which is consistent with the SEM-EDS results (Table S1†).

The XRD profiles of LMO series materials are presented in Fig. S2.† All LMO series materials present Li_2MnO_3-like diffraction patterns in the range of 10°–90°, leading to the monoclinic phase (space group *C*2/*m*).[7,40] The Rietveld-refined XRD data for the LMO material is presented in Fig. 2e, and the unit cell parameters calculated by the General Structure Analysis System (GSAS) are listed in Tables S2 and S3.† For

Table 1 Target *vs.* measured Li : Mn : La atomic ratio of pristine and modified materials by ICP-AES

Material	Target Li : Mn : La	Measured Li : Mn : La
LMO	2.00 : 1.00 : 0.00	2.021 : 1.011 : 0.000
$La_{0.01}$	2.00 : 0.99 : 0.01	2.008 : 0.992 : 0.011
$La_{0.03}$	2.00 : 0.97 : 0.03	2.011 : 0.971 : 0.031
$La_{0.05}$	2.00 : 0.95 : 0.05	2.020 : 0.952 : 0.052
LMLO	2.00 : 1.97 : 0.03	2.010 : 1.973 : 0.031

© 2024 The Author(s). Published by the Royal Society of Chemistry

Open Access Article. Published on 25 November 2024. Downloaded on 2/10/2026 6:33:09 PM. This article is licensed under a Creative Commons Attribution-NonCommercial 3.0 Unported Licence.

pristine LMO material, the peaks at about 18° are characteristic of a layered rhombohedral $LiMO_2$ phase, the relatively weak reflections between 20° and 23° are assigned as the Li_2MnO_3-like phase (Fig. 2e and S1†). For the XRD patterns of LMLO material (Fig. 2f), the extra diffraction peaks at 36.4° and 44.2° can be attributed to the spinel $Li_2Mn_4O_9$ phase (or some spinel-like phases),[34] which indicates that the modified material delivers a layered-spinel biphase, consistent with the TEM results. The extra peak at about 33° for the LMLO material may come from the La-containing compound, which needs further confirmation.

Electrochemical performance

The electrochemical activity was detected *via* galvanostatic charge–discharge measurement. The initial charge–discharge curves for LMO series materials are presented in Fig. 3a. Under a voltage window of 1.5–4.8 V, the pristine LMO electrode presents a characteristic 4.5 V voltage plateau during charging, which is associated with the activation process and delivers a discharge capacity of 57.4 mA h g^{-1}.[8] After La doping, the discharge capacity increases to 72.1 mA h g^{-1}, 182.8 mA h g^{-1}, and 99.6 mA h g^{-1} for $La_{0.01}$, $La_{0.03}$, and $La_{0.05}$ electrodes, respectively. This indicates the positive effect of La doping on the electrochemical performance. It is worth noting that the modified LMLO material delivers an extremely enhanced capacity of 233.4 mA h g^{-1} and special charge–discharge curves with new discharge voltage plateaus at 4.0 V and 2.8 V, which are characteristic features for the spinel phase.[41] The enhanced reversible capacity in the LMLO material suggests suppressed irreversible oxygen release after the synergistic modification. The cycling performance of the LMO series was obtained with a current density of 25 mA g^{-1} in the voltage range between 2.0 V and 4.8 V (Fig. 3b). It shows that the LMLO material delivers higher capacity than that of the other three materials during the whole cycling process. The discharge capacities of the pristine and La-modified materials gradually increase in the initial 10 cycles, which can be ascribed to a gradual activation process to utilize more lithium ions.[42,43] At the 100th charge–discharge cycle, the available capacity for LMO and LMLO is 13.5 mA h g^{-1} and 118.1 mA h g^{-1}, respectively. It is worth noting that the capacity decay remains obvious upon extensive cycles in LMO systems. The conventional LMO delivers poor cycling, which is related to Mn dissolution, surface interaction, structural evolution, *etc.*[30,44,45] Further improvements could be gained through other modifications such as surface coating, which is beyond the scope of this work.

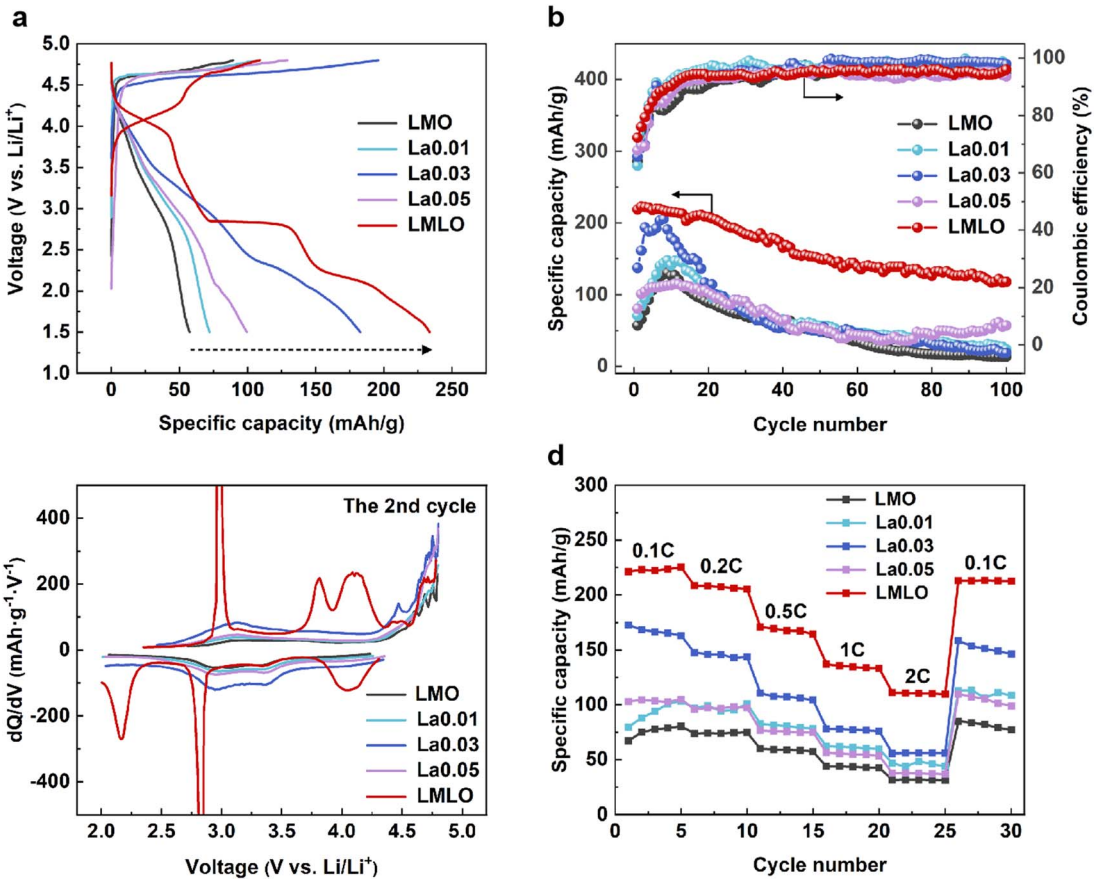

Fig. 3 Galvanostatic charge–discharge curves for LMO series cathodes. (a) Initial charge–discharge curves with voltage between 4.8 V and 1.5 V at a current density of 25 mA g^{-1}. (b) Specific capacity and coulombic efficiency evolution during the cycling process with voltage between 4.8 V and 2.0 V. (c) d*Q*/d*V* curves for the 2nd cycle. (d) Rate performance.

© 2024 The Author(s). Published by the Royal Society of Chemistry

Open Access Article. Published on 25 November 2024. Downloaded on 2/10/2026 6:33:09 PM.
This article is licensed under a Creative Commons Attribution-NonCommercial 3.0 Unported Licence.

Differential capacity against voltage (dQ/dV) curves for LMO series materials under the voltage range of 2.0–4.8 V were analyzed (Fig. 3c). After the activation process in the initial cycle, the pristine LMO electrode delivers a broad hump due to the partial overlap of cathodic and anionic redox. The peak pairs at the 2.5–4.4 V region belong to the redox of Mn^{2+}/Mn^{4+} in the layered cathode material.[46] Above 4.5 V, the peak pairs mainly belong to the oxygen redox reaction.[14] For comparison, the modified LMLO electrode presents peak pairs at about 3.0 V and 4.0 V, indicating that the spinel phase exists in the LMLO material. As for the rate performance, LMO series materials were evaluated between 2.0 V and 4.8 V with 0.1 C, 0.2 C, 0.5 C, 1 C, and 2 C rates (1 C = 200 mA g^{-1}), respectively (Fig. 3d). The La-modified materials deliver higher specific capacity than that of the pristine LMO at all rates. When cycled at 2 C rate, the available capacity for LMO and LMLO is 31.5 mA h g^{-1} and 111.1 mA h g^{-1}, respectively. Upon returning to the 0.1 C rate, the LMLO material ensures a capacity of 213.0 mA h g^{-1}, which is 251% that for the LMO material (85.0 mA h g^{-1}).

To explore the effect of La doping and Li/Mn optimization, the charge–discharge curves during the cycling process for LMO and LMLO electrodes were compared (Fig. S3†). It is notable that during the cycling process, the charge curves for the Mn-rich LMO electrode change to S-type curves. For the LMLO electrode, the initial charge–discharge curves contain the specific 4.0 V and 2.8 V discharge voltage plateaus, which are well sustained during cycling, suggesting the coexistence of layered phase and spinel phase in the modified LMLO material.

The corresponding differential capacity against voltage (dQ/dV) curves for LMO and LMLO at different cycles under the voltage range of 2.0–4.8 V were further analyzed (Fig. S3c and d†). Pristine LMO delivers an oxidation peak at about 4.5 V, which can be linked to the activation of the Li_2MnO_3 component accompanied by irreversible oxygen release.[47] Besides, the anodic peaks (at about 3.0 V) gradually shift to lower potential during cycling, indicating a sharp voltage decay with increasing cycle number for pristine LMO (Fig. S3c†). For comparison, the peaks at about 2.8 V (discharge process) are maintained well for the LMLO material during the cycling process (Fig. S3d†). The comparison of the normalized charge–discharge profiles is presented in Fig. S4.† The pristine LMO shows severe voltage decay upon cycling (Fig. S4a†). The voltage decay has been ascribed to the structural degradation, low-voltage redox couples, and so on.[48] In contrast, the modified LMLO material presents improved voltage evolution (Fig. S4b†), which supports the advantage of synergetic modification.

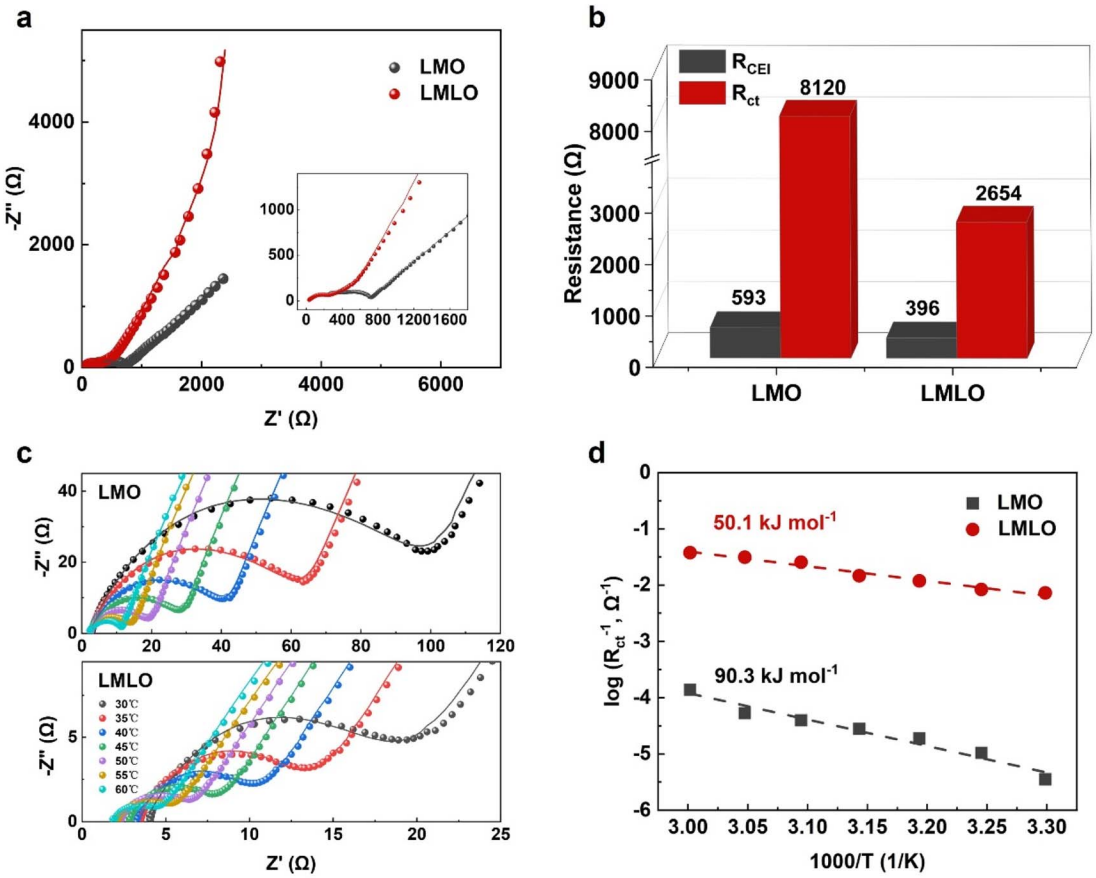

Fig. 4 (a) Nyquist plots of the EIS data for LMO and LMLO materials after 100 cycles and (b) corresponding fitting results of R_{CEI} and R_{ct}. (c) R_{ct} obtained from variable temperature EIS data for LMO and LMLO materials and (d) corresponding activation energy (E_a) of the charge transfer process.

© 2024 The Author(s). Published by the Royal Society of Chemistry

Open Access Article. Published on 25 November 2024. Downloaded on 2/10/2026 6:33:09 PM.
This article is licensed under a Creative Commons Attribution-NonCommercial 3.0 Unported Licence.

Electrochemical characterization

To study the Li-ion transport behavior under synergetic modification, the EIS technique for cells after 100 cycles was examined to investigate the Li^+ transfer property (Fig. 4a).[28] The EIS spectra were fitted based on the equivalent circuit model (Fig. S5†), and the corresponding fitting data is shown in Fig. 4b.[49] It shows that the R_{ct} in LMLO is lower than that in LMO material, which is a good explanation for the better rate capability gained above. The reduced R_{ct} would come from the reduced interfacial side reaction after layered-spinel phases modification.

To further study the impact of modification on the charge transfer process, EIS at varied temperatures was adopted to monitor the cell impedance (Fig. 4c and S6†). The values of R_{ct} can be obtained *via* equivalent circuit fitting from Nyquist profiles at different temperatures (Table S4†).[49] According to the Arrhenius relationship that charge transfer resistance (R_{ct}) follows (Note S1†), the value of activation energy (E_a) could be obtained.[50] As shown in Fig. 4d, the calculated E_a for LMO and LMLO electrodes is 90.3 kJ mol^{-1} and 50.1 kJ mol^{-1}, respectively. This indicates that the synergistic La doping and Li/Mn optimization could effectively enhance the kinetics of lithium-ion diffusion. The facilitated Li^+ transport across the electrolyte/electrode interface should be attributed to the stabilized structure and mitigated side reaction.

Cyclic voltammetry at different scan rates (ranging from 0.3 mV s^{-1} to 1.1 mV s^{-1}) was carried out to investigate the Li^+ diffusion kinetics (Fig. 5a and b). The Li^+ diffusion coefficients of LMO and LMLO were evaluated by following the Randles–Sevcik equation

$$I_p = 2.69 \times 10^5 n^{3/2} A D^{1/2} v^{1/2} C_0 \quad (1)$$

where n refers to the number of electrons transferred per molecule (1.0 for lithium ions), A refers to the surface area of the cathode, and C_0 refers to the bulk concentration of lithium ions.[51] Hence, by fitting the I_p–$v^{1/2}$ curve and comparing the slope, the apparent diffusion kinetics of the materials can be well contrasted. As plotted in Fig. 5c and d, the anodic peak current slope of the LMLO electrode is 0.0287, which is higher than that of the LMO electrode (0.0204). As for the cathodic peak current, the slope of the LMLO electrode (0.0245) is higher than that of the LMO electrode (0.0228). It indicates faster lithium-ion transportation kinetics *via* bulk modification, which is consistent with the improved rate performance and enhanced cycling stability.

The kinetics of the redox reactions that take place during the charge/discharge process was further verified by the galvanostatic intermittent titration technique (GITT, Fig. 6a). In the GITT test, a short current pulse was applied and then removed, followed by a sharp voltage increase (decrease) and achievement

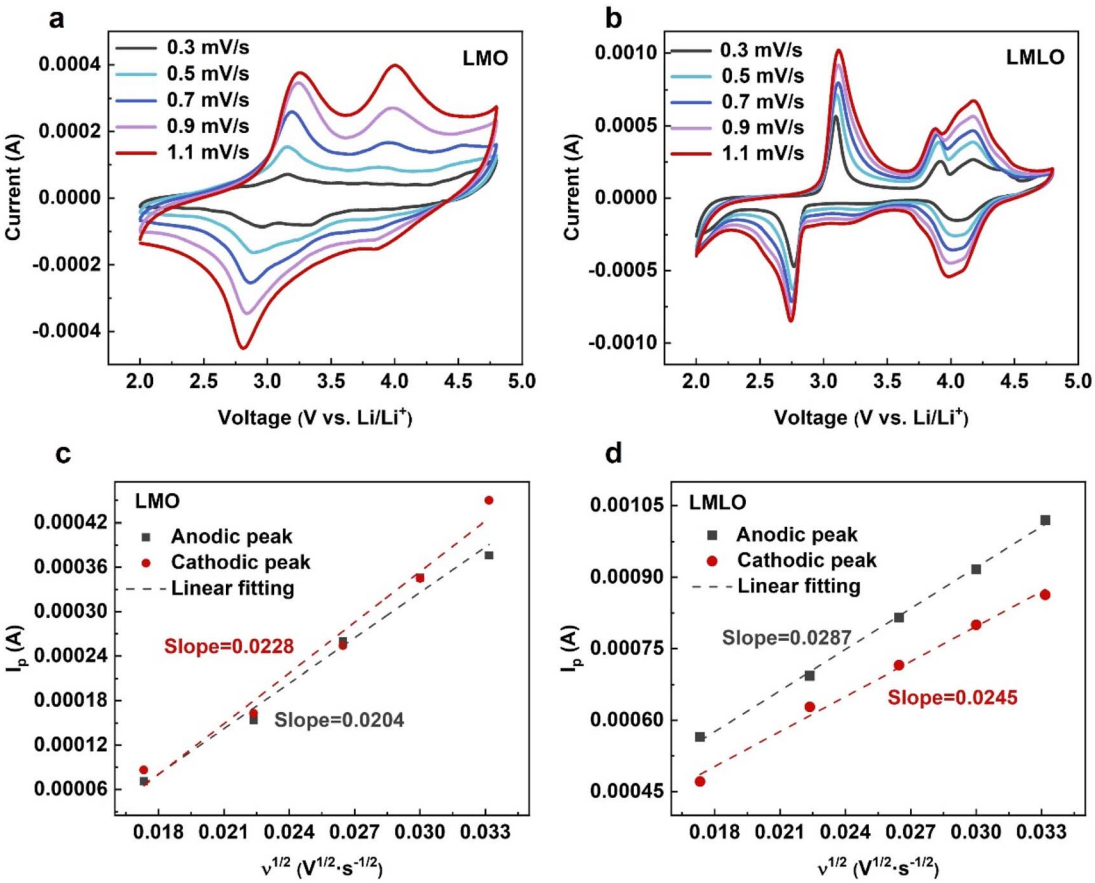

Fig. 5 CV curves for (a) LMO and (b) LMLO with different scan rates. The corresponding I_p–$v^{1/2}$ profiles for (c) LMO and (d) LMLO materials.

Open Access Article. Published on 25 November 2024. Downloaded on 2/10/2026 6:33:09 PM.
This article is licensed under a Creative Commons Attribution-NonCommercial 3.0 Unported Licence.

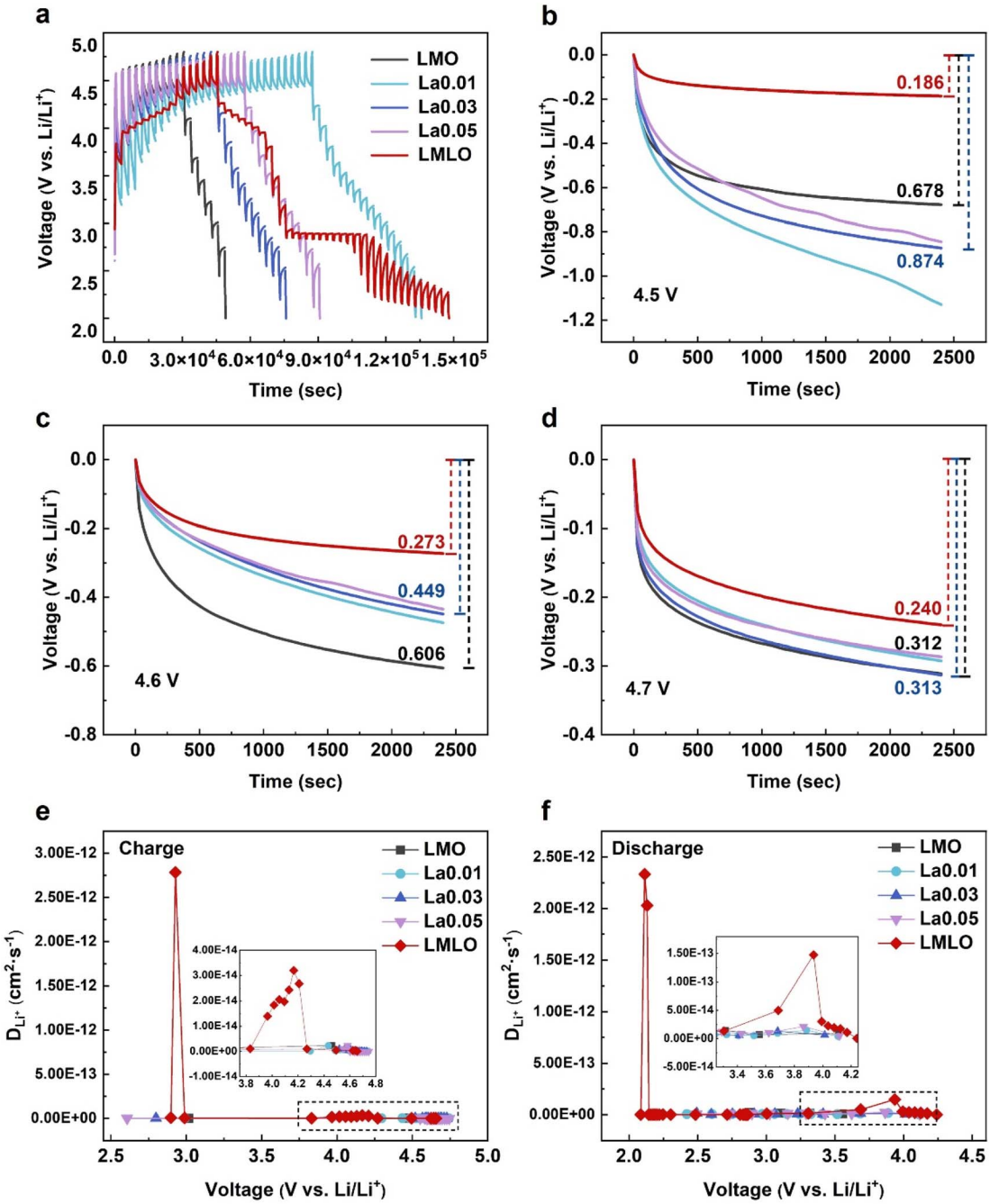

Fig. 6 Hysteresis and kinetics of LMO series cathodes. (a) GITT voltage profiles for LMO series materials. (b–d) Time-elapsed OCV during rest periods at various voltages depicted in (a). D_{Li^+} for (e) the charge process and (f) the discharge process from the GITT data in (a).

of the thermodynamic equilibrium potential. The kinetics of lithium-ion diffusion could be investigated by comparing the overpotential between the initial state and the final state of the open circuit voltage (OCV) test at the selected voltage.[52] As shown in Fig. 6b, LMLO delivers a smaller potential drop (186 mV) than that of pristine LMO (678 mV) at a voltage of about 4.5 V. The difference in the OCV value clearly shows accelerated kinetics of lithium-ion diffusion for LMLO in the 4.5 V region. Upon charging to a higher voltage (Fig. 6c and d), the lower overpotential (273 mV for 4.6 V, 240 mV for 4.7 V) for the LMLO electrode than that of the pristine LMO electrode (606 mV for 4.6 V, 312 mV for 4.7 V) also confirms the positive effect of the modification. Here, based on the equation

$$D_{Li^+} = \frac{4}{\pi\tau}\left(\frac{m_B V_M}{M_B A}\right)^2\left(\frac{\Delta E_s}{\Delta E_\tau}\right)^2 \quad (2)$$

a series of D_{Li^+} values *versus* charge/discharge voltage was generated (Fig. 6e and f).[53] The results show that the modified LMLO electrode delivers enhanced D_{Li^+} value.

© 2024 The Author(s). Published by the Royal Society of Chemistry

Open Access Article. Published on 25 November 2024. Downloaded on 2/10/2026 6:33:09 PM.
This article is licensed under a Creative Commons Attribution-NonCommercial 3.0 Unported Licence.

Structural evolution after modification

Thermal stability is an important indicator for practical application.[54] The DSC measurements were conducted with LMO and LMLO materials charged to 4.8 V. As shown in Fig. 7a, the LMO electrode presents a large exothermic peak at 228 °C with a high heat flow of 29.3 J g^{-1}, while the main peak for LMLO electrode shifts to a higher temperature of 239 °C with a much lower heat flow of 5.0 J g^{-1}. This result reveals that lanthurizing and Li/Mn optimization can significantly improve the thermal stability of the Mn-rich LMO cathode.

To confirm the formation of spinel phases, Raman spectra were obtained for the LMO and LMLO materials (Fig. 7b).[33,55,56] The Raman band appearing at about 400 cm^{-1} can be assigned to the monoclinic Li_2MnO_3 phase. The other two significant Raman peaks appear at about 473 and 593 cm^{-1} in the spectra, which results from the bending E_g and stretching A_{1g} modes in the Li_2MnO_3 phase, respectively. It is worth noting that the LMLO material delivers a new peak at about 630 cm^{-1}, which can be attributed to the spinel phase. It indicates the mixed structure of the layered and spinel phases after modification, which consists of the XRD patterns.

To understand the mechanism of how the spinel phase improves the cycling performance, the structural evolution during charge–discharge was monitored. Fig. 7c and d show the *ex situ* XRD results corresponding to the (003) reflections, representing the unit cell change along the *c*-axis. In Fig. 7c, the (003) reflection of LMO shifts to a lower angle when charged to 4.1 V, which is likely caused by the coulombic repulsion of the anion layers. Besides, the (003) reflection of LMO splits into two peaks at a voltage of 4.1 V, indicating the appearance of a new phase. With further Li^+ removal (charge to 4.5 V, 4.8 V), the (003) reflections undergo an aggressive shift to higher angles, suggesting a drastic contraction of the *c*-axis due to the phase transition. For comparison, the modified LMLO delivers a more stable peak evolution upon cycling (Fig. 7d). Upon discharge to 2.0 V, the (003) reflection of LMO shifts to a lower angle, which is lower than that of LMLO.

In addition, the batteries were cycled for 5 cycles, and the positive electrodes were taken out for the XRD tests. In Fig. 7c,

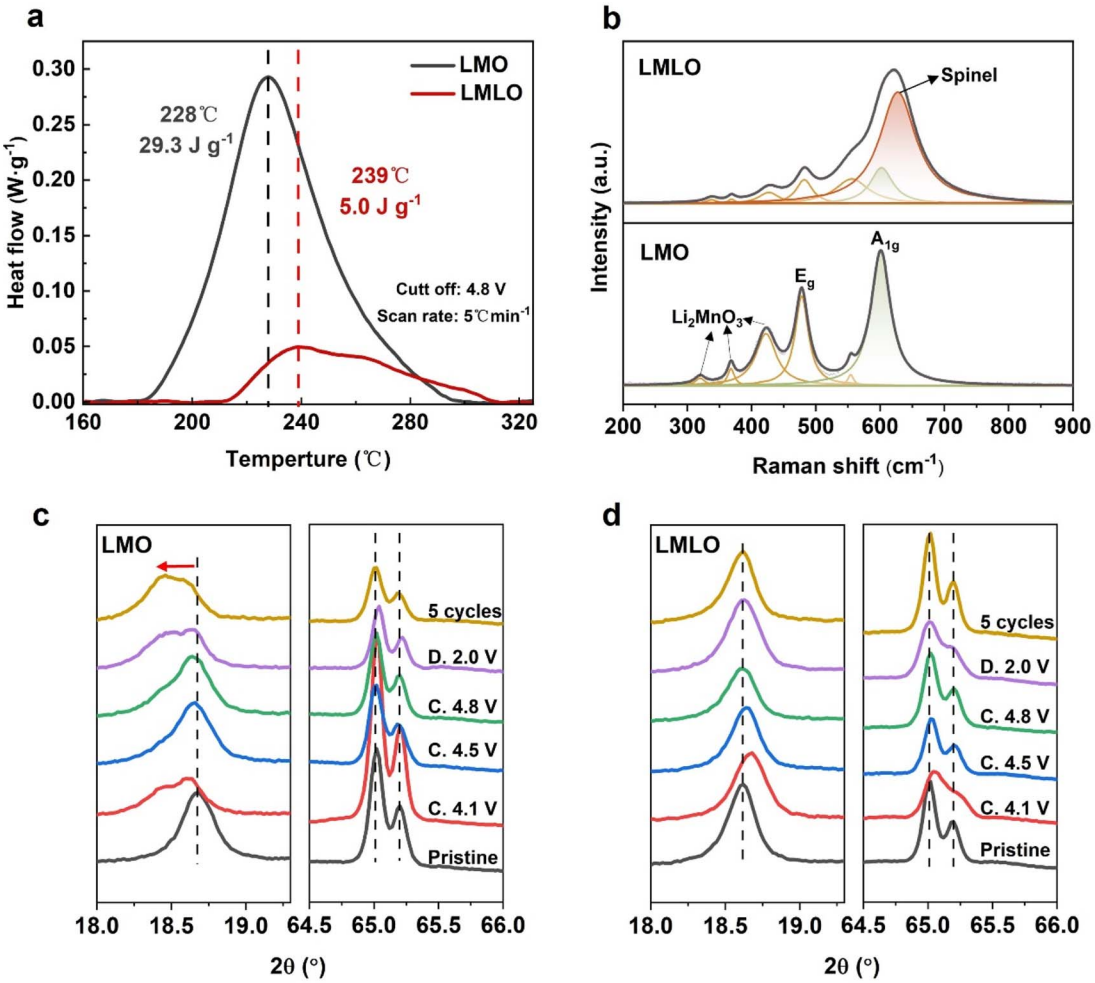

Fig. 7 Structural evolution for the modified material. (a) Differential scanning calorimetry data for charged LMO and LMLO electrodes. (b) Raman spectra of LMO and LMLO materials. (c and d) The *ex situ* XRD patterns for (c) LMO material and (d) LMLO material in the pristine state, initial charge–discharge process, and after cycling.

Open Access Article. Published on 25 November 2024. Downloaded on 2/10/2026 6:33:09 PM. This article is licensed under a Creative Commons Attribution-NonCommercial 3.0 Unported Licence.

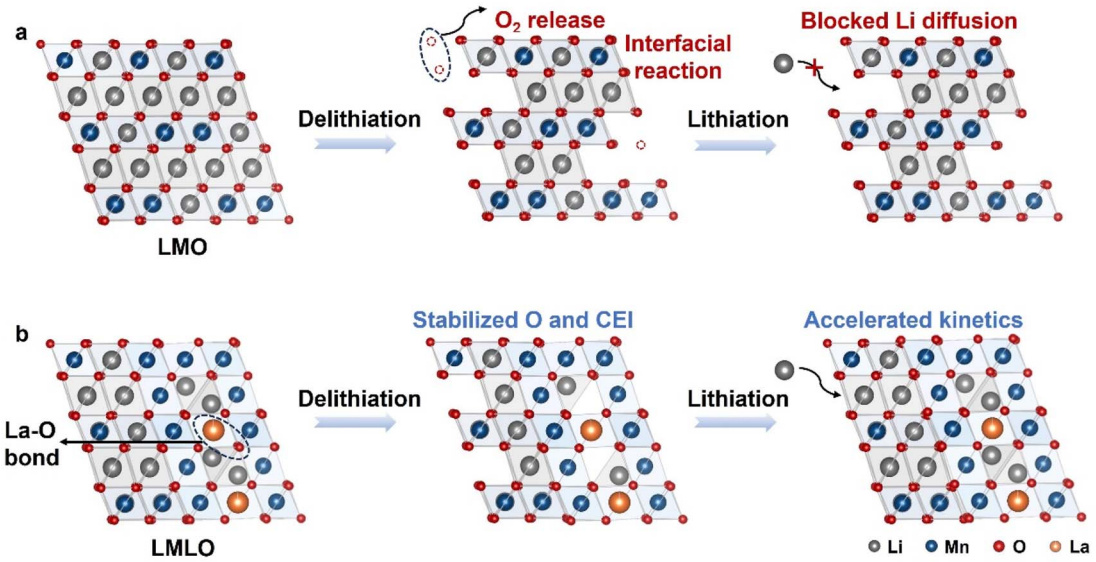

Fig. 8 Proposed mechanism of (a) LMO and (b) LMLO materials during the electrochemical process.

the (003) reflections of the LMO samples shifted to a lower diffraction angle after 5 cycles. In detail, the (003) reflections of LMO contain a broad shoulder, which is mainly due to the presence of two different phases with close lattice parameters, indicating that a two-phase transition reaction occurs in LMO. As for LMLO, the almost identical shape of the (003) reflections indicates a quasi-single-phase process (Fig. 7d). The continuous single-phase reaction makes lattice contraction to have a buffer process, thus reducing the structural damage. The (003) reflection of LMLO is well sustained, suggesting that the modified LMLO has a more enhanced reversible lattice shrinkage, which is favorable for maintaining the structural integrity during electrochemical cycling.

Based on the characterization results, Fig. 8 proposes the synergistic effect of modification during electrochemical cycling. Pristine LMO material delivers limited capacity due to sluggish kinetics and is accompanied by interfacial side reaction (Fig. 8a). For comparison, a spinel phase is *in situ* formed and coexists with the bulk layered phase on the modified material (Fig. 8b). The layered-spinel biphase ensures accelerated kinetics, as evidenced by the GITT, CV and EIS results. Besides, the biphase with stabilized La–O bond would mitigate the irreversible oxygen release, which suppresses the interfacial side reaction and further enhances the available capacity. Meanwhile, during the cycling process, the structural evolution is stabilized after modification, as evidenced by the *ex situ* XRD data.

Conclusions

To summarize, we have demonstrated a synergistic approach for accelerated kinetics and for realizing high-capacity cycling. We showed that the modified LMLO phase can enhance the Li-ion diffusion. Electrochemical characterization demonstrated that the modified Mn-rich cathode could deliver an enhanced available capacity of 233.4 mA h g^{-1} at a voltage of 1.5–4.8 V. Our lanthurizing and delithiation approach accelerates the lithium-ion diffusion kinetics and widens the strategies for enhancing the energy density.

Declarations

The author declares that there is no relevant competitive economic interest or personal relationship between them that will hinder the work of this article.

Data availability

The authors confirm that the data supporting the findings of this study are available within the article and its ESI.†

Conflicts of interest

The authors declare no competing financial interest.

Acknowledgements

This research was financially supported by Zhuhai Natural Science Foundation (Grant no. ZH22017003210080PWC), Science Foundation of Faculty of Comprehensive Health Industry (no. 2023DJKCY013), Zhuhai College of Science and Technology Three Levels Talent Construction Project, and College Students' Innovation and Entrepreneurship Training Program (202413684009X, DC2024084).

References

1 W. Lee, S. Muhammad, C. Sergey, H. Lee, J. Yoon, Y. M. Kang and W. S. Yoon, Advances in the cathode materials for

© 2024 The Author(s). Published by the Royal Society of Chemistry

Open Access Article. Published on 25 November 2024. Downloaded on 2/10/2026 6:33:09 PM. This article is licensed under a Creative Commons Attribution-NonCommercial 3.0 Unported Licence.

lithium rechargeable batteries, *Angew. Chem., Int. Ed.*, 2020, **59**(7), 2578–2605.
2 T. Kim, W. Song, D.-Y. Son, L. K. Ono and Y. Qi, Lithium-ion batteries: outlook on present, future, and hybridized technologies, *J. Mater. Chem. A*, 2019, **7**(7), 2942–2964.
3 J. Zheng, S. Myeong, W. Cho, P. Yan, J. Xiao, C. Wang, J. Cho and J. G. Zhang, Li-and Mn-rich cathode materials: challenges to commercialization, *Adv. Energy Mater.*, 2017, **7**(6), 1601284.
4 Y. Chen, Z. Xie, Q. Lv, N. Zhu, S. Shang, N. Wang, Y. Jin and W. Yan, Facilitating structural stability of the Li-rich layered cathode materials by cation rearrangements and Li vacancies, *Appl. Surf. Sci.*, 2023, **639**, 158203.
5 L. Zeng, H. Liang, B. Qiu, Z. Shi, S. Cheng, K. Shi, Q. Liu and Z. Liu, Voltage decay of Li-rich layered oxides: mechanism, modification strategies, and perspectives, *Adv. Funct. Mater.*, 2023, **33**(25), 2213260.
6 W. Yang, Oxygen release and oxygen redox, *Nat. Energy*, 2018, **3**(8), 619–620.
7 B. Qiu, M. Zhang, Y. Xia, Z. Liu and Y. S. Meng, Understanding and controlling anionic electrochemical activity in high-capacity oxides for next generation Li-ion batteries, *Chem. Mater.*, 2017, **29**(3), 908–915.
8 S. Kang, D. Choi, H. Lee, B. Choi and Y.-M. Kang, A mechanistic insight into the oxygen redox of Li-rich layered cathodes and their related electronic/atomic behaviors upon cycling, *Adv. Mater.*, 2023, **35**(43), 2211965.
9 S. Sharifi-Asl, J. Lu, K. Amine and R. Shahbazian-Yassar, Oxygen release degradation in Li-ion battery cathode materials: mechanisms and mitigating approaches, *Adv. Energy Mater.*, 2019, **9**(22), 1900551.
10 S. Saha, G. Assat, M. T. Sougrati, D. Foix, H. Li, J. Vergnet, S. Turi, Y. Ha, W. Yang and J. Cabana, Exploring the bottlenecks of anionic redox in Li-rich layered sulfides, *Nat. Energy*, 2019, **4**(11), 977–987.
11 E. McCalla, A. M. Abakumov, M. Saubanère, D. Foix, E. J. Berg, G. Rousse, M.-L. Doublet, D. Gonbeau, P. Novák and G. Van Tendeloo, Visualization of O-O peroxo-like dimers in high-capacity layered oxides for Li-ion batteries, *Science*, 2015, **350**(6267), 1516–1521.
12 K. Zhou, S. Zheng, H. Liu, C. Zhang, H. Gao, M. Luo, N. Xu, Y. Xiang, X. Liu, G. Zhong and Y. Yang, Elucidating and mitigating the degradation of cationic-anionic redox processes in $Li_{1.2}Mn_{0.4}Ti_{0.4}O_2$ cation-disordered cathode materials, *ACS Appl. Mater. Interfaces*, 2019, **11**(49), 45674–45682.
13 S. Liu, H. Yue, Y. Mo, L. Luo, X. Wu, S. Yang, Y. Huang and G. Yuan, Retarding the capacity fading and voltage decay of Li-rich Mn-based cathode materials via a compatible layer coating for high-performance lithium-ion batteries, *RSC Adv.*, 2024, **14**(36), 26142–26151.
14 X. He, J. Wu, Z. Zhu, H. Liu, N. Li, D. Zhou, X. Zhou, H. Zhang, D. Bresser, Y. Fu, M. J. Crafton, B. D. McCloskey, Y. Chen, K. An, P. Liu, A. Jain, J. Li, W. Yang, Y. Yang, M. Winter and R. Kostecki, Chemical and structural evolution of Li-Mn-rich layered electrodes under different current densities, *Energy Environ. Sci.*, 2022, **15**, 4137.
15 Q. Li, Z. Yao, E. Lee, Y. Xu, M. M. Thackeray, C. Wolverton, V. P. Dravid and J. Wu, Dynamic imaging of crystalline defects in lithium-manganese oxide electrodes during electrochemical activation to high voltage, *Nat. Commun.*, 2019, **10**(1), 1692.
16 X. D. Zhang, J. L. Shi, J. Y. Liang, Y. X. Yin, J. N. Zhang, X. Q. Yu and Y. G. Guo, Suppressing surface lattice oxygen release of Li-rich cathode materials via heterostructured spinel $Li_4Mn_5O_{12}$ coating, *Adv. Mater.*, 2018, **30**(29), 1801751.
17 X. Qu, H. Huang, T. Wan, L. Hu, Z. Yu, Y. Liu, A. Dou, Y. Zhou, M. Su, X. Peng, H.-H. Wu, T. Wu and D. Chu, An integrated surface coating strategy to enhance the electrochemical performance of nickel-rich layered cathodes, *Nano Energy*, 2022, **91**, 106665.
18 J. Wu, Z. Chen, J. Cheng, Q. Wen, W. Gao, X. Wang and C. Tuo, Accelerating Li^+ intercalation kinetics through synergetic modification in Li-rich cathode, *J. Mater. Sci.*, 2023, **58**, 16785–16796.
19 B. M. de Boisse, J. Jang, M. Okubo and A. Yamada, Cobalt-free O2-type lithium-rich layered oxides, *J. Electrochem. Soc.*, 2018, **165**(16), A3630–A3633.
20 X. Li, Y. Qiao, S. Guo, K. Jiang, M. Ishida and H. Zhou, A new type of Li-rich rock-salt oxide $Li_2Ni_{1/3}Ru_{2/3}O_3$ with reversible anionic redox chemistry, *Adv. Mater.*, 2019, **31**(11), 1807825.
21 D. Liu, X. Fan, Z. Li, T. Liu, M. Sun, C. Qian, M. Ling, Y. Liu and C. Liang, A cation/anion co-doped $Li_{1.12}Na_{0.08}Ni_{0.2}Mn_{0.6}O_{1.95}F_{0.05}$ cathode for lithium ion batteries, *Nano Energy*, 2019, **58**, 786–796.
22 K. Xu, Electrolytes and interphases in Li-ion batteries and beyond, *Chem. Rev.*, 2014, **114**(23), 11503–11618.
23 Y. Wu, K. Zhou, F. Ren, Y. Ha, Z. Liang, X. Zheng, Z. Wang, W. Yang, M. Zhang, M. Luo, C. Battaglia, W. Yang, L. Zhu, Z. Gong and Y. Yang, Highly reversible Li_2RuO_3 cathodes in sulfide-based all solid-state lithium batteries, *Energy Environ. Sci.*, 2022, **15**(8), 3470–3482.
24 X. Qu, Z. Yu, D. Ruan, A. Dou, M. Su, Y. Zhou, Y. Liu and D. Chu, Enhanced electrochemical performance of Ni-rich cathode materials with $Li_{1.3}Al_{0.3}Ti_{1.7}(PO_4)_3$ coating, *ACS Sustain. Chem. Eng.*, 2020, **8**(15), 5819–5830.
25 S. Wang, Y. Li, J. Wu, B. Zheng, M. J. McDonald and Y. Yang, Toward a stabilized lattice framework and surface structure of layered lithium-rich cathode materials with Ti modification, *Phys. Chem. Chem. Phys.*, 2015, **17**(15), 10151–10159.
26 C.-C. Wang and A. Manthiram, Influence of cationic substitutions on the first charge and reversible capacities of lithium-rich layered oxide cathodes, *J. Mater. Chem. A*, 2013, **1**(35), 10209–10217.
27 R. Yu, X. Wang, Y. Fu, L. Wang, S. Cai, M. Liu, B. Lu, G. Wang, D. Wang and Q. Ren, Effect of magnesium doping on properties of lithium-rich layered oxide cathodes based on a one-step co-precipitation strategy, *J. Mater. Chem. A*, 2016, **4**(13), 4941–4951.
28 X. Yang, M. Lin, G. Zheng, J. Wu, X. Wang, F. Ren, W. Zhang, Y. Liao, W. Zhao, Z. Zhang, N. Xu, W. Yang and Y. Yang,

Open Access Article. Published on 25 November 2024. Downloaded on 2/10/2026 6:33:09 PM. This article is licensed under a Creative Commons Attribution-NonCommercial 3.0 Unported Licence.

Enabling stable high-voltage $LiCoO_2$ operation by using synergetic interfacial modification strategy, *Adv. Funct. Mater.*, 2020, **30**(43), 2004664.

29 J. Rana, J. K. Papp, Z. Lebens-Higgins, M. Zuba, L. A. Kaufman, A. Goel, R. Schmuch, M. Winter, M. S. Whittingham, W. Yang, B. D. McCloskey and L. F. J. Piper, Quantifying the capacity contributions during activation of Li_2MnO_3, *ACS Energy Lett.*, 2020, **5**(2), 634–641.

30 J. Wu, X. Zhang, S. Zheng, H. Liu, J. Wu, R. Fu, Y. Li, Y. Xiang, R. Liu, W. Zuo, Z. Cui, Q. Wu, S. Wu, Z. Chen, P. Liu, W. Yang and Y. Yang, Tuning oxygen redox reaction through inductive effect with proton insertion in Li-rich oxides, *ACS Appl. Mater. Interfaces*, 2020, **12**(6), 7277–7284.

31 M. Cai, Y. Dong, M. Xie, W. Dong, C. Dong, P. Dai, H. Zhang, X. Wang, X. Sun, S. Zhang, M. Yoon, H. Xu, Y. Ge, J. Li and F. Huang, Stalling oxygen evolution in high-voltage cathodes by lanthurization, *Nat. Energy*, 2023, **8**(2), 159–168.

32 J. Wan, J. Zhu, Y. Xiang, G. Zhong, X. Liu, Y. Li, K. H. L. Zhang, C. Hong, J. Zheng, K. Wang and Y. Yang, Revealing the correlation between structure evolution and electrochemical performance of high-voltage lithium cobalt oxide, *J. Energy Chem.*, 2021, **54**, 786–794.

33 J. Wu, Z. Cui, J. Wu, Y. Xiang, H. Liu, S. Zheng, W. Yang and Y. Yang, Suppression of voltage-decay in Li_2MnO_3 cathode via reconstruction of layered-spinel coexisting phases, *J. Mater. Chem. A*, 2020, **8**(36), 18687–18697.

34 Y. J. Hao, Q. Y. Lai, L. Wang, X.-Y. Xu and H. Y. Chu, Electrochemical performance of a high cation-deficiency $Li_2Mn_4O_9$/active carbon supercapacitor in $LiNO_3$ electrolyte, *Synth. Met.*, 2010, **160**(7), 669–674.

35 B. H. Toby, EXPGUI, a graphical user interface for GSAS, *J. Appl. Crystallogr.*, 2001, **34**(2), 210–213.

36 K. Momma and F. Izumi, VESTA 3 for three-dimensional visualization of crystal, volumetric and morphology data, *J. Appl. Crystallogr.*, 2011, **44**, 1272–1276.

37 T. Matsunaga, H. Komatsu, K. Shimoda, T. Minato, M. Yonemura, T. Kamiyama, S. Kobayash, T. Kato, T. Hirayama, Y. Ikuhara, H. Arai, Y. Ukyo, Y. Uchimoto and Z. Ogumi, Dependence of structural defects in Li_2MnO_3 on synthesis temperature, *Chem. Mater.*, 2016, **28**(12), 4143–4150.

38 D. Luo, X. Ding, J. Fan, Z. Zhang, P. Liu, X. Yang, J. Guo, S. Sun and Z. Lin, Accurate control of initial coulombic efficiency for lithium-rich manganese-based layered oxides by surface multicomponent integration, *Angew. Chem., Int. Ed.*, 2020, **59**(51), 23061–23066.

39 X.-D. Zhang, J.-L. Shi, J.-Y. Liang, Y.-X. Yin, J.-N. Zhang, X.-Q. Yu and Y.-G. Guo, Suppressing surface lattice oxygen release of Li-rich cathode materials via heterostructured spinel $Li_4Mn_5O_{12}$ coating, *Adv. Mater.*, 2018, **30**(29), 1801751.

40 C. Delmas, C. Fouassier and P. Hagenmuller, Structural classification and properties of the layered oxides, *Physica B+C*, 1980, **99**(1), 81–85.

41 J. B. Goodenough and K.-S. Park, The Li-ion rechargeable battery: a perspective, *J. Am. Chem. Soc.*, 2013, **135**(4), 1167–1176.

42 L. Xiao, J. Xiao, X. Yu, P. Yan, J. Zheng, M. Engelhard, P. Bhattacharya, C. Wang, X.-Q. Yang and J.-G. Zhang, Effects of structural defects on the electrochemical activation of Li_2MnO_3, *Nano Energy*, 2015, **16**, 143–151.

43 P. Yan, L. Xiao, J. Zheng, Y. Zhou, Y. He, X. Zu, S. X. Mao, J. Xiao, F. Gao and J.-G. Zhang, Probing the degradation mechanism of Li_2MnO_3 cathode for Li-ion batteries, *Chem. Mater.*, 2015, **27**(3), 975–982.

44 F. Dogan, J. R. Croy, M. Balasubramanian, M. D. Slater, H. Iddir, C. S. Johnson, J. T. Vaughey and B. Key, Solid state NMR studies of Li_2MnO_3 and Li-rich cathode materials: proton insertion, local structure, and voltage fade, *J. Electrochem. Soc.*, 2015, **162**(1), A235–A243.

45 Y. Denis, K. Yanagida, Y. Kato and H. Nakamura, Electrochemical activities in Li_2MnO_3, *J. Electrochem. Soc.*, 2009, **156**(6), A417–A424.

46 D. Luo, H. Zhu, Y. Xia, Z. Yin, Y. Qin, T. Li, Q. Zhang, L. Gu, Y. Peng, J. Zhang, K. M. Wiaderek, Y. Huang, T. Yang, Y. Tang, S. Lan, Y. Ren, W. Lu, C. M. Wolverton and Q. Liu, A Li-rich layered oxide cathode with negligible voltage decay, *Nat. Energy*, 2023, **8**, 1078–1087.

47 X. H. Zhang, S. Cao, R. Z. Yu, C. Li, Y. Huang, Y. Wang, X. Y. Wang and G. R. Chen, Improving electrochemical performances of Li-rich layered Mn-based oxide cathodes through $K_2Cr_2O_7$ solution treatment, *ACS Appl. Energy Mater.*, 2019, **2**(2), 1563–1571.

48 E. Hu, X. Yu, R. Lin, X. Bi, J. Lu, S. Bak, K.-W. Nam, H. L. Xin, C. Jaye, D. A. Fischer, K. Amine and X.-Q. Yang, Evolution of redox couples in Li- and Mn-rich cathode materials and mitigation of voltage fade by reducing oxygen release, *Nat. Energy*, 2018, **3**(8), 690–698.

49 W. Dudan, W. Fei, Z. Huanhuan, L. Yupeng, Y. Nachuan and C. Kanghua, Electrochemical performance improvement of Li_2MnO_3 cathode materials by MgF_2 coating, *J. Electrochem.*, 2020, **26**(2), 289–297.

50 W. Zhang, X. Sun, Y. Tang, H. Xia, Y. Zeng, L. Qiao, Z. Zhu, Z. Lv, Y. Zhang, X. Ge, S. Xi, Z. Wang, Y. Du and X. Chen, Lowering charge transfer barrier of $LiMn_2O_4$ via nickel surface doping to enhance Li^+ intercalation kinetics at subzero temperatures, *J. Am. Chem. Soc.*, 2019, **141**(36), 14038–14042.

51 Y. Wei, J. Cheng, D. Li, Z. Zeng, H. Liu, H. Zhang, F. Ji, X. Geng, J. Lu and L. Ci, A structure self-healing Li-rich cathode achieved by lithium supplement of Li-rich LLZO coating, *Adv. Funct. Mater.*, 2023, **33**(22), 2214775.

52 Y. Yue, N. Li, L. Li, E. E. Foley, Y. Fu, V. S. Battaglia, R. J. Clément, C. Wang and W. Tong, Redox behaviors in a Li-excess cation-disordered Mn–Nb–O–F rocksalt cathode, *Chem. Mater.*, 2020, **32**(11), 4490–4498.

53 S. Lou, Q. Liu, F. Zhang, Q. Liu, Z. Yu, T. Mu, Y. Zhao, J. Borovilas, Y. Chen, M. Ge, X. Xiao, W.-K. Lee, G. Yin, Y. Yang, X. Sun and J. Wang, Insights into interfacial effect and local lithium-ion transport in polycrystalline cathodes of solid-state batteries, *Nat. Commun.*, 2020, **11**(1), 5700.

54 Q. Fan, K. Lin, S. Yang, S. Guan, J. Chen, S. Feng, J. Liu, L. Liu, J. Li and Z. Shi, Constructing effective TiO_2 nano-coating for high-voltage Ni-rich cathode materials for

© 2024 The Author(s). Published by the Royal Society of Chemistry

Open Access Article. Published on 25 November 2024. Downloaded on 2/10/2026 6:33:09 PM.
This article is licensed under a Creative Commons Attribution-NonCommercial 3.0 Unported Licence.

lithium ion batteries by precise kinetic control, *J. Power Sources*, 2020, **477**(30), 228745.

55 C. M. Julien and M. Massot, Lattice vibrations of materials for lithium rechargeable batteries III. Lithium manganese oxides, *Mater. Sci. Eng., B*, 2003, **100**(1), 69–78.

56 C. S. Johnson, N. Li, J. T. Vaughey, S. A. Hackney and M. M. Thackeray, Lithium–manganese oxide electrodes with layered–spinel composite structures $xLi_2MnO_3 \cdot (1-x)Li_{1+y}Mn_{2-y}O_4$ ($0<x<1$, $0 \leqslant y \leqslant 0.33$) for lithium batteries, *Electrochem. Commun.*, 2005, **7**(5), 528–536.